

INTEGRAL FIELD SPECTROSCOPY OF AGN ABSORPTION OUTFLOWS: MRK 509 AND IRAS F04250–5718

GUILIN LIU^{1,†}, NAHUM ARAV¹ AND DAVID S. N. RUPKE²

¹Department of Physics, Virginia Tech, Blacksburg, VA 24061, USA and

²Department of Physics, Rhodes College, Memphis, TN 38112, USA

Accepted for publication in ApJS on September 16, 2015

ABSTRACT

Ultraviolet (UV) absorption lines provide abundant spectroscopic information enabling the probe of the physical conditions in AGN outflows, but the outflow radii (and the energetics consequently) can only be determined indirectly. We present the first direct test of these determinations using integral field unit (IFU) spectroscopy. We have conducted Gemini IFU mapping of the ionized gas nebulae surrounding two AGNs, whose outflow radii have been constrained by UV absorption line analyses. In Mrk 509, we find a quasi-spherical outflow with a radius of 1.2 kpc and a velocity of $\sim 290 \text{ km s}^{-1}$, while IRAS F04250–5718 is driving a biconical outflow extending out to 2.9 kpc, with a velocity of $\sim 580 \text{ km s}^{-1}$ and an opening angle of $\sim 70^\circ$. The derived mass flow rate is ~ 5 and $> 1 M_\odot \text{ yr}^{-1}$, respectively, and the kinetic luminosity is $\gtrsim 1 \times 10^{41} \text{ erg s}^{-1}$ for both. Adopting the outflow radii and geometric parameters measured from IFU, absorption line analyses would yield mass flow rates and kinetic luminosities in agreement with the above results within a factor of ~ 2 . We conclude that the spatial locations, kinematics and energetics revealed by this IFU emission-line study are consistent with pre-existing UV absorption line analyses, providing a long-awaited direct confirmation of the latter as an effective approach for characterizing outflow properties.

Subject headings: quasars: individual (Mrk 509, IRAS F04250–5718) — quasars: emission lines — quasars: absorption lines

1. INTRODUCTION

The active phase of the super-massive black holes residing in galaxy centers has crucial effects on the global properties of their host galaxies. Thus, feedback from active galactic nuclei (AGNs) has become an indispensable ingredient of galaxy formation models, requiring the black holes to blow large-scale outflowing winds which clear out the surrounding gas and prevent future star formation (e.g. Tabor & Binney 1993; Di Matteo et al. 2005; Hopkins & Elvis 2010). Roughly 20–40% of quasars show blueshifted broad absorption lines (BAL), implying that sub-relativistic quasar outflows are ubiquitous (Hewett & Foltz 2003; Ganguly & Brotherton 2008; Knigge et al. 2008; Dai et al. 2008). Theoretical modeling has shown that massive, wide angle outflows can indeed be very efficient feedback agents (e.g. Ostriker et al. 2010; Ciotti et al. 2010; Soker 2010; McCarthy et al. 2010; Hopkins & Elvis 2010; Faucher-Giguère et al. 2012; Choi et al. 2014).

Over the last decade, our collaboration and other research groups have been performing absorption line analyses on about 20 AGN absorption outflows to measure the distance from the central source, the mass flow rate and kinetic luminosity (Hamann et al. 2001; de Kool et al. 2001, 2002a,b; Gabel et al. 2005; Moe et al. 2009; Bautista et al. 2010; Dunn et al. 2010; Aoki et al. 2011; Arav et al. 2012; Borguet et al. 2012a,b, 2013; Edmonds et al. 2011; Arav et al. 2013; Lucy et al. 2014; Chamberlain et al. 2015). Our state-of-the-art analysis methods are able to determine the outflow sizes to better than a factor of two

(Bautista et al. 2010), frequently finding them located at kpc scales (see Arav et al. 2013 for a review), comparable to the spatial extent of the host galaxies. The main weakness of these investigations, obtained by ultraviolet (UV) spectroscopy of excited transitions coupled with detailed photoionization modeling, is the lack of spatial information. The indirectly inferred outflow sizes remain to be confirmed, not to mention their morphology and spatial structure.

In recent years, integral field unit (IFU) observations have been conducted to map the ionized gas surrounding AGNs (e.g. Nesvadba et al. 2008; Husemann et al. 2008; Fu & Stockton 2009; Lipari et al. 2009; Alexander et al. 2010; Humphrey et al. 2010; Rupke & Veilleux 2011; Husemann et al. 2011; Cano-Díaz et al. 2012; Harrison et al. 2012; Westmoquette et al. 2012; Husemann et al. 2013; Liu et al. 2013a,b; Rupke & Veilleux 2013; Harrison et al. 2014; Liu et al. 2014; Shih & Stockton 2014; McElroy et al. 2015; Davies et al. 2015). In particular, this technique has enabled us to detect massive, powerful, kpc-scale, AGN-driven outflows both in radio-quiet major mergers (Rupke & Veilleux 2011, 2013) and in high luminosity radio-quiet type 2 (Liu et al. 2013a,b) and type 1 (Liu et al. 2014) quasars, providing evidence for ubiquitous galaxy-wide feedback in luminous quasars.

IFU spectroscopy has the obvious advantage of directly measuring the spatial extent of the outflows which can only be derived indirectly from absorption line analyses (not to mention the morphology and the spatial distribution of gas kinematics that can only be obtained with IFU), yet the latter provides more abundant spectroscopic information covering a wide range of ionization and density, enabling the probe of the physical con-

[†] Email: glliu@vt.edu

ditions in the multi-phase outflowing gas (Arav et al. 2013). Therefore, IFU mapping of outflowing AGNs will directly test the outflow locations derived from UV absorption lines, providing a strong constraint on the physical assumptions and parameters of the outflow models.

In this paper, we present Gemini IFU mapping of the ionized gas nebulae around two bright radio-quiet active galaxies, Mrk 509 and IRAS F04250–5718. The locations of their outflows both have been determined or constrained by previous UV absorption line analyses using high-quality spectroscopy.

Although spectroscopically classified as Seyfert 1.5 galaxies (Table 1), Mrk 509 and IRAS F04250–5718 both reside close to the quasar/Seyfert galaxy borderline (Kopylov et al. 1974; Véron-Cetty & Véron 2006), and are thus deemed low-luminosity quasars. As one of the best studied AGNs, Mrk 509 ($z = 0.03440$ Huchra et al. 1993) has been scrutinized in multiple windows of its electromagnetic spectrum (a thorough description of its observational properties is available in Kaastra et al. 2011). Combining HST/COS data from a massive multi-wavelength monitoring campaign (see Kaastra et al. 2011) and archival HST/STIS data, Arav et al. (2012) analyzed all the kinematic components of its outflow and obtained a lower limit of 100–200 pc for their galactocentric distance.

IRAS F04250–5718 ($z = 0.104$, Thomas et al. 1998) was discovered in X-ray as 1H 0419–577 Wood et al. 1984, and is also known as LB 1727 and 1ES 0425–573. So far, the X-ray spectral energy distribution has been the primary interest of the existing studies on it (the reader is referred to the introduction section of Edmonds et al. (2011) for a detailed description of its observational history). Edmonds et al. (2011) identified three kinematic components from its HST/COS UV spectra, and determined a conservative lower limit of 3 kpc for the outflow. The basic characteristics of these two objects and the observing information of our observations are summarized in Table 1.

This paper is organized as follows. In Section 2, we describe the observations and reduction of our data. Flux calibration, PSF subtraction and line fitting are presented in Section 3. Outflow features are identified and characterized in Section 4. In Section 5, we measure the spatial scales and derive physical velocities of the outflows, and compare to absorption line analyses. The mass flow rates and kinetic luminosities are estimated in Section 6, followed by a summary in Section 7. We adopt an $h = 0.70$, $\Omega_m = 0.29$, $\Omega_\Lambda = 0.71$ cosmology throughout this paper.

2. OBSERVATIONS AND DATA REDUCTION

We observed the program targets with the Gemini-South telescope between 2013 July and 2014 January (program ID: GS-2013B-Q-84, PI: D. Rupke; we also observed IRAS F22456–5125 in our campaign, but the data quality is insufficient for deriving useful results). We used the 1-slit Integral Field Unit (IFU) mode on GMOS-S, so that the wavelength coverage is optimized. We performed two exposures, separated by a spatial dithering of 1.5'' along the shorter axis of the field of view (FoV). Combining the dithered exposures, we cover a final FoV

of $5'' \times 5''$, translating to a linear scale of 3.5×3.5 kpc² for Mrk 509 and 9.5×9.5 kpc² for IRAS F04250–5718. The science FoV, sampled by 1000 contiguous 0.2''-diameter hexagonal lenslets, is interpolated to a finer grid (0.1'') in the final data products.

The seeing at the observing site was 0.6''–0.7'', measured from the point spread function (PSF) model we construct from the continuum emission (see Section 3.2). We used the spectroscopy blocking filter GG455-G0329 in our program. The central wavelength of the employed grating B600-G5323 was set to 625 nm for IRAS F04250–5718 and 615 nm for Mrk 509, respectively. This grating has a spectral resolution of $R \sim 2300$ at these wavelengths. Both objects were observed between 4700Å and 7600Å so as to cover the [O III]-H β region. To accurately determine the spectral resolution, we perform Gaussian fits on unresolved sky lines in the [O III]-H β neighborhood, finding their full width at half maximum (FWHM) to be ~ 120 km s⁻¹. The emission lines of interest ([O III] $\lambda\lambda$ 5007, 4959Å, H β , H α , [N II] $\lambda\lambda$ 6548, 6583Å) are all well resolved. Table 1 summarizes our Gemini observations.

We use the Gemini package for IRAF² to reduce the data, following the standard procedure for GMOS IFU described in the tasks *gmosinfoifu* and *gmosexamples* with slight modification (detailed in Liu et al. 2013a). The datacube product reduced from each exposure has 0.1'' spatial pixels (“spaxels”). We finally combine the two frames using the task *imcombine* by taking the mean spectra in each spaxel. The [O III]5007Å line is well detected in every spatial position, with signal-to-noise ratios at its peak of 10–20 at the FoV edges, and 2500–2800 in the FoV centers.

3. IFU DATA ANALYSIS

3.1. Flux calibration and continuum / Fe II subtraction

We flux-calibrate our data against previous spectroscopic measurements. For IRAS F04250–5718, Guainazzi et al. (1998) find an integrated [O III] flux of $f_{[\text{O III}]} = 5.0 \times 10^{-13}$ erg s⁻¹ cm⁻² using the ESO 1.52m telescope equipped with an 8''-wide long slit, while a 5-year coordinated program of spectroscopic monitoring of Mrk 509 reports $f_{[\text{O III}]} = 6.79 \times 10^{-13}$ erg s⁻¹ cm⁻² using various apertures sizes, of which the smallest is $5'' \times 8''$ (Carone et al. 1996). Flux loss from these measurements are deemed negligible because the employed apertures are larger than our field of view.

In order to remove the contamination from Fe II emission, we perform a procedure identical to Liu et al. (2014). We fit the continua in the [O III]-H β neighborhood with the sum of two components: a quadratic polynomial, and the Fe II template from Boroson & Green (1992) smoothed using a Gaussian kernel whose width is one of the free fitting parameters. However, we note that Fe II contamination to our [O III] analysis is insignificant in both targets.

3.2. PSF subtraction

² The Image Reduction and Analysis Facility (IRAF) is distributed by the National Optical Astronomy Observatories which is operated by the Association of Universities for Research in Astronomy, Inc. under cooperative agreement with the National Science Foundation.

Table 1
Characteristics of the sample objects and observational parameters.

Object (1)	α, δ (J2000.0) (2)	z (3)	Type (4)	PA (5)	t_{exp} (6)	Seeing (7)	$L_{[\text{O III}]}$ (8)	$\Sigma_{[\text{O III}],\text{peak}}$ (9)
Mrk 509	20 ^h 44 ^m 09 ^s .7 − 10° 43′ 24″.5	0.0344	Seyfert 1.5	0°	1200×2	0″.70	1.9×10 ⁴²	4.9×10 ^{−13}
IRAS F04250−5718	04 ^h 26 ^m 00 ^s .7 − 57° 12′ 01″.0	0.104	Seyfert 1.5	90°	1600×2	0″.62	1.4×10 ⁴³	2.5×10 ^{−13}

Note. — (1) Object name. (2) Right ascension and declination. (3) Redshifts are taken from Thomas et al. (1998, for IRAS F04250−5718) and Huchra et al. (1993, for Mrk 509). (4) AGN type, from the NASA/IPAC Extragalactic Database (NED, <http://ned.ipac.caltech.edu>). (5) Position angle of the field of view, measured by the longer (5″) axis of the FoV (1-slit IFU) from north to east. (6) Exposure time (in seconds) and number of exposures. (7) Seeing at the observing site (FWHM). (8) Total luminosity of the [O III] λ 5007 Å line (erg s^{−1}), from observations by Guainazzi et al. (1998, for IRAS F04250−5718) and Carone et al. (1996, for Mrk 509). (9) Peak [O III] λ 5007 Å surface brightness before PSF subtraction (erg s^{−1} cm^{−2} arcsec^{−2}).

Our program was undertaken when seeing at the observing site was 0.6″–0.7″, requiring careful analysis of our datasets to minimize the effects of the PSF. The observations become significantly easier to interpret if the PSF is carefully modeled and subtracted from the IFU datacube. The most reliable approach is constructing PSF models from the real data themselves.

Quasar light scattered by the interstellar matter (Borguet et al. 2008) or star formation in the quasar host (Letawe et al. 2007; Silverman et al. 2009) might both contribute to the continuum emission. However, we assume that the continuum emission is dominated by a central point source in this work. This is a reasonable assumption for both of our targets that are classified as type 1 AGNs, and is further validated by the fact that the FoV is only larger than the FWHM of the PSF by a factor of 6, and thus the scattered light from the host galaxy, if detectable at all in the outer regions, is overwhelmed by the broad wings of the PSF.

To construct a PSF model in an optimized way, we first select three rest-frame wavelength intervals free of [O III] and H β line emission, 4925–4945Å, 4970–4980Å and 5020–5050Å, normalize the central brightest pixel to unity, then create a median image for each interval. For where [O III] and H β emission exist, we linearly interpolate between each pair of adjacent median images to construct the PSF model at each wavelength, so that a PSF model datacube is created. These constructed PSFs have an FWHM of 0.62″ for IRAS F04250−5718 and 0.70″ for Mrk 509.

For the [O III]–H β region, we perform Gaussian fits to both the PSF model at each wavelength and to the corresponding slice image to compute their centroids using the GCNTRD routine in the IDL Astronomy User’s Library³ (Gaussian fits are sufficient for our purpose of centroiding only). We then align the PSF to the slice image using the obtained centroids (although the position of the AGN is fixed in the sky, we allow the peak of the PSF to move minimally in the plane of the sky (within one spatial pixel, 0.1″) for optimized results). After that, the PSF is scaled to the central peak brightness of the slice image, and subtracted from the latter. As the last step, guided by these automated algorithms, we manually adjust the brightness of the PSF to further correct imperfect subtractions.

3.3. Spectral line fits

After removing Fe II emission and subtracting the PSF from the IFU datacubes, we perform multi-Gaussian fits to the [O III] λ 5007,4959 doublet, so that a noiseless model of the line in every spatial pixel is attained, a procedure identical to Liu et al. (2013b). As described in that paper, up to 3 Gaussian components are needed for good fits so that the reduced $\chi^2 \lesssim 2$ in every spatial pixel, and the actual number of employed Gaussians is determined by comparing their respective reduced χ^2 values. We then compute the [O III] line intensity in every spatial position from the multi-Gaussian fit (instead of the observed profile). The surface brightness sensitivity of our [O III] surface brightness maps is measured to be $\sigma_{[\text{O III}]} = (3\text{--}6) \times 10^{-17}$ erg s^{−1} cm^{−2} arcsec^{−2}.

As in Liu et al. (2013b), we do not assign physical meanings to the individual Gaussians (with the sole exception of decomposing [O III] to remove the tidal tail emission in Mrk 509, see Section 4.2). The fits are merely used to produce noiseless models of the [O III] line to facilitate non-parametric measurements.

Following Whittle (1985) and Liu et al. (2013b), we measure two quantities that characterize the line-of-sight velocity and velocity dispersion of the ionized gas, the median velocity (v_{med}) that bisects the total area underneath the [O III] emission line profile, and the velocity interval that encloses 80% of the total [O III] emission centered at the median velocity (W_{80}). As noted in those papers, W_{80} is more sensitive to the weak broad wings of a non-Gaussian profile, but is similar to FWHM of a Gaussian velocity profile ($W_{80} = 1.088 \times \text{FWHM}$).

4. OUTFLOW SIGNATURES

4.1. IRAS F04250−5718

The [O III] surface brightness, median velocity and W_{80} maps are shown in Figure 1. A pair of strong [O III]-emitting blobs reside in both sides of the central AGN (the central black pixels are due to slight over-subtraction), featuring the prevalent bi-conical structure of the AGN ionization in low-redshift active galaxies (e.g. Fischer et al. 2013). The roughly vertical gap between the two blobs therefore marks the distribution of obscuring material with opacity higher than inside the [O III] blobs. This picture is well consistent with the median velocity map on which the distribution of its highest and lowest velocities clearly depict a rotation pattern remarkably similar to a highly inclined ($i \gtrsim 70^\circ$) disk galaxy (to confirm this judgement, we use the publicly

³ <http://idlastro.gsfc.nasa.gov/>

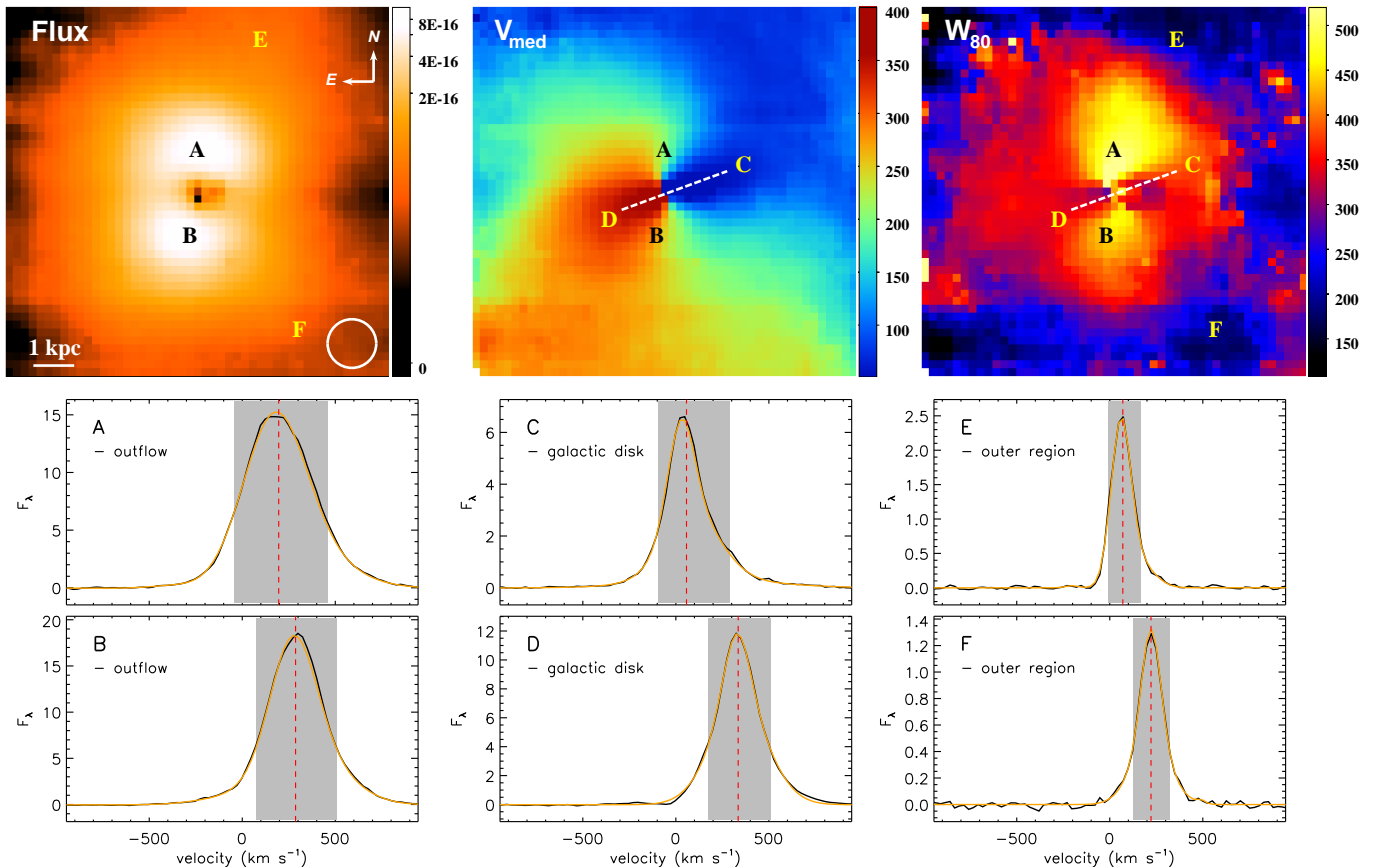


Figure 1. IRAS F04250–5718. **Top color maps.** Maps of the $[\text{O III}]\lambda 5007 \text{ \AA}$ surface brightness (left, in units of $\text{erg s}^{-1} \text{ cm}^{-2} \text{ arcsec}^{-2}$, logarithmic scale), median velocity (middle, in km s^{-1}) and line width (W_{80} , right, in km s^{-1}). The seeing at the observing site is depicted by the open circle on the surface brightness map. The white dashed line on the V_{med} and W_{80} maps marks the orientation of the nearly edge-on galactic disk rotating at $\sim 170 \text{ km s}^{-1}$. **Bottom spectra.** We select 6 spatial positions to present the $[\text{O III}]$ velocity profile therein (F_{λ} is in units of $10^{-17} \text{ erg s}^{-1} \text{ cm}^{-2} \text{ \AA}^{-1}$, within a $0.1''$ spatial pixel), including 2 outflow regions (“A”, “B”), 2 galactic disk regions (“C”, “D”), and two outer regions (“E”, “F”). The fitted line is in orange, the median velocity is marked by red dashed lines, and the velocity range used for calculating W_{80} is denoted by grey boxes.

available software DISKFIT (Spekkens & Sellwood 2007; Sellwood & Sánchez 2010; Kuzio de Naray et al. 2012) to fit the velocity field of the central region to a rotating disk model, finding an inclination angle of $i = 70^{\circ} \pm 10^{\circ}$). Half of the maximum velocity difference on the v_{med} map is 170 km s^{-1} , approximating the line-of-sight rotation speed of a typical edge-on disk galaxy, which extends along the direction $\sim 20^{\circ}$ from top to the right.

The W_{80} maps reveal a pair of prominent high-line-width lobes. This structure spatially coincides with the off-center brightness peaks seen in the $[\text{O III}]$ intensity map, and extends in a direction (nearly horizontal in the figure) $\sim 60^{\circ}$ from the direction of maximum W_{med} difference which appears to fall in a low line-width valley (the contours marking approximately the maximum and minimum v_{med} values are overlaid on the W_{80} map to guide the eyes). The line width of the pair of lobes reach as high as $W_{80} \sim 400\text{--}500 \text{ km s}^{-1}$, strongly pointing to being highly turbulent outflowing gas (cf. discussion in Liu et al. 2013b).

Therefore, the three maps in Figure 1 are in consistency with a simple and familiar physical picture: the AGN resides in the center of a nearly edge-on disk galaxy with a rotation speed of $\sim 200 \text{ km s}^{-1}$, which both obscures its photoionization along the direction of the disk

so that the surrounding gas forms a wide ($\gtrsim 120^{\circ}$) photoionization bi-cone, and forces the galactic wind to propagate into other directions with less obstruction. It is unclear why the outflow is tilted $\sim 20^{\circ}$ off the axis of the rotating disk. Possible explanations include a warped galaxy disk, or a detailed matter distribution with further complication that is not revealed by our observations.

High $[\text{O III}]$ linewidth implies outflowing ionized gas, both because of the bulk motion of the gas, and more plausibly, because of the broad distribution of the velocity of the narrow-line clouds embedded in the winds (see discussion in Liu et al. 2013b). In view of the uniform W_{80} value inside the galactic disk (spanning a narrow range of $280\text{--}320 \text{ km s}^{-1}$ over the narrow region where V_{med} reaches its minimum and maximum, Fig. 1), we conservatively choose the $W_{80}=320 \text{ km s}^{-1}$ contour as representing the boundary of the galactic outflow. The furthest galactocentric distance that the outflow reaches is then measured to be $1.5''$, translating to 2.9 kpc , on the more extended side, and $1.1''$ or 2.1 kpc on the more compact side.

These distances should be deemed as lower limits. The $[\text{O III}]$ line emission is strongly detected in the entire $10 \times 10 \text{ kpc}^2$ field of view, thus the possibility cannot

be ruled out that W_{80} falls below 320 km s^{-1} when the wind propagates to sufficiently large distances and even become undetectable. Further more, galactic winds are multi-phase and our observation only traces the warm ionized gas. A volume-filling, high-temperature, low density ionized gas phase has long been proposed (Heckman et al. 1990), which may be physically even more extended and cannot be traced by [O III] emission. Projection effects also lead to underestimating the physical scale if the outflow does not perfectly lie in the plane of the sky. In spite of these uncertainties, the basic conclusion is validated that an outflow with a total physical extent of at least 5 kpc is exerting feedback effects on galaxy-wide scales.

4.2. Mrk 509

Mrk 509 is a more complicated system than F04250, and interpreting the [O III] nonparametric measurements is nontrivial. In particular, the HST FQ508N narrow-band [O III] imaging (Figure 2, Fischer et al. 2013, 2015) detects tidal structures featured by a prominent linear tail extending out to a length of $7.8''$ (5.4 kpc) that appears to abruptly bend toward the nucleus from the southwest. Fischer et al. (2013) suggest that the positive velocity of the southwest structure is indicative of inflowing, rendering the system a minor merger with a dwarf galaxy. These features are also spatially resolved by our IFU observations, which becomes more evident after careful PSF subtraction (detailed in Section 3.2), and makes characterizing outflow features a challenging task (Figure 3, top row).

The [O III] line shows unambiguous double-peak profiles in the west $\sim 40\%$ fraction of the FoV. The two peaks are well separated wherever the tidal tail dominates the [O III] emission: the bluer peak always corresponds to a negative velocity (between -180 and -100 km s^{-1}), and the redder peak persistently shows a positive velocity (70 – 220 km s^{-1}). We therefore perform 2-Gaussian fits to the velocity profile of the [O III] line in every spatial pixel of this region to decompose their respective spatial structures.

This approach results in a clear and physical decomposition demonstrated in Figure 3. The intensity map of the Gaussian peaking at a bluer wavelength reconstructs the morphology of the linear tidal tail precisely, whose narrow linewidth (typically $W_{80} \sim 200 \text{ km s}^{-1}$) throughout the region is also consistent with being an gaseous structure illuminated by the central AGN (middle row; see discussion in Liu et al. 2013b and Liu et al. 2009). The intensity map of the redder Gaussian reveals a “southwestern jut” mentioned in Fischer et al. (2013) with little contamination from the tail (bottom row).

Here we interpret the “southwestern jut” as part of the galactic outflow (see other possibilities and a discussion of the complex gas kinematics in Section 6.2). This is not only because of the wholeness, smoothness and symmetry of [O III] flux when it is mosaiced with the original data for the rest of the FoV (Figure 3, bottom row), but more importantly, because the ratio of [O III] to the narrow $H\beta$ component is as high as 13 on average (same as that in the center) which indicates high ionization state caused by AGN emission routinely found in photoionization cones (see Section 6.1; Liu et al. 2013a), and because the mosaiced W_{80} map shows behaviors similar to known

outflowing objects (see below).

Broad line widths are indicative of gaseous outflows in IFU data, as reasoned by Liu et al. (2013b), in which the [O III]-emitting clouds possess a wide local velocity distribution in addition to the global outflow kinematics, leading to broad wings of the [O III] line profile. In absence of the tidal tail, we are left with a structure with elliptical or roughly round morphology shown by the [O III] flux, with relatively high W_{80} values distributed in a roundish region. The situation here is similar to the luminous $z \sim 0.5$ SDSS quasars observed by Liu et al. (2013b). In those objects, high linewidths persist at a roughly constant level in the central several kpc ($W_{80} \sim 500$ – 2000 km s^{-1}) which often decrease to much lower values (~ 100 – 200 km s^{-1}) in the outer regions (several kpc from the center) beyond the direct impact of the outflow.

In Mrk 509, W_{80} declines rapidly at $\sim 310 \text{ km s}^{-1}$ in the eastern 60% of the FoV, and at $\sim 220 \text{ km s}^{-1}$ in the region where the tidal tail feature is removed through decomposition. Because 2-Gaussian fits cannot account for the broad base of the [O III] line in this region, W_{80} measured there may be underestimated. Whether or not taking into account this part of the FoV, we measure the northeastern extent of the outflow (where we are the most certain about its outflow characteristic due to the observed suppressed narrow $H\beta$ line, see discussion in Section 5), and find a radius of 1.2 kpc ($1.7''$) for this roughly spherical (or very wide angle) outflow.

5. COMPARE TO ABSORPTION LINE ANALYSES

5.1. IRAS F04250–5718

5.1.1. Spatial extent

The galactocentric distance of the outflow revealed by our Gemini data, $R \gtrsim 2.9$ kpc and $R \gtrsim 2.2$ kpc for the two sides of the bi-conical outflow, is consistent with the previous UV absorption line analysis obtained by our group, $R \gtrsim 3$ kpc Edmonds et al. (2011). In that paper, we measured the column density of C II and an upper limit on the column density of C II*, and determined the electron density in the outflow to be $\lesssim 30 \text{ cm}^{-3}$. Combined with photoionization modeling, we found the above constraint for the outflow radius. The direct IFU mapping in this work provides the first ever direct test that validates our approach to indirectly derive the outflow size, which has been applied on nearly 20 objects during the last decade (see Arav et al. 2013 for a review).

5.1.2. Gas Kinematics

Liu et al. (2013b) proposed a spherical, extinction-free outflow model with a constant physical velocity as a representative picture for the quasi-spherical outflows seen in their luminous quasars at $z \sim 0.5$. For such a simplistic model, the radial velocity profile remains exactly the same for the entire system (see Equation 10 therein), rendering the observed linewidth a constant across the W_{80} map. As discussed in Section 4, the outflow from IRAS F04250–5718 clearly shows bi-conical structures. The opening angle measured from the high W_{80} regions (Figure 1) is $\sim 70^\circ$ for both cones. The spherical model is not directly applicable to this system, but the calculation in that paper can be utilized here.

As in Figure 1 we do not observe an limb-brightened outflow (expected for a hollow-cone structure where

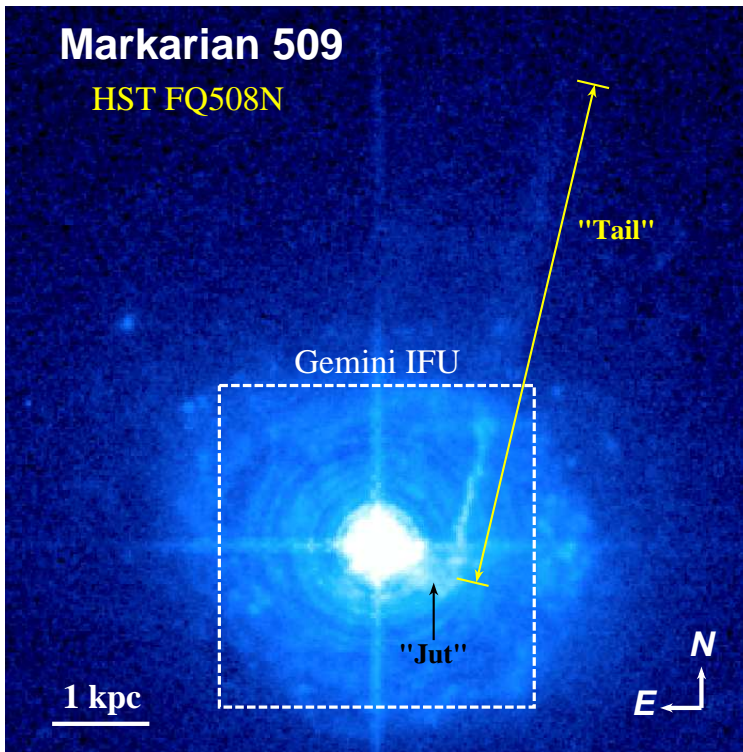


Figure 2. HST archival [O III] narrow-band image of Mrk 509 (GO-12212; PI: D. Crenshaw). The yellow box depicts the $5'' \times 5''$ field of view of our Gemini IFU observation. The spectacular 5.4-kpc-long linear “tail” structure and the “southwestern jut” that appears to connect it to the center are also marked. See Section 4.2 for discussion of these structures.

the walls of the cones dominate the emission; e.g. Crenshaw et al. 2000), we assume a filled bicone model equivalent to part of a spherically symmetric outflow, in which the luminosity density only depends on the spherical radius r , and scales as a power law, $j(r) \propto r^{-\alpha}$. The very high inclination of the galactic disk (see Section 4) allows us to assume that the biconical outflow (roughly perpendicular to the galactic disk) to lie approximately in the plane of the sky.

In this model, the maximum linewidth is achieved on the axis of the bicone. If we further assume a constant outflow velocity v_0 , the calculation for a spherical model in (Liu et al. 2013b, Section 4.1, Equations 7, 8 and 9) remains valid. Although the conclusion therein that the radial velocity profile remains the same at every spatial position is no longer applicable, on the axis of the bicone, Equation (10) in that paper only requires a trivial modification,

$$I(v_z, R_{\parallel}) \propto R_{\parallel}^{1-\alpha} \left[1 - \left(\frac{v_z}{v_0 \sin \frac{\theta}{2}} \right) \right]^{(\alpha-3)/2}, \quad (1)$$

where I is the [O III] flux at a given spatial position and a given wavelength corresponding to v_z , the line-of-sight component of the outflow velocity \mathbf{v}_0 , R_{\parallel} is the projected 2-dimensional radius from the center along the outflow axis (in the plane of the sky under our assumption), θ is the opening angle of each cone ($\sim 70^\circ$),

In the outer region ($R_{\parallel} \gtrsim 1.3$ kpc) of the quasar nebula along the outflow axis, the observed [O III] surface brightness indeed closely follows a power-law relation $I \propto R_{\parallel}^{-3.0 \pm 0.1}$, therefore $\alpha = 4.0$ as per our best fits. Inserting these parameters into Equation 1, we find a

simple linear relationship between W_{80} and v_0 ,

$$W_{80} = 1.374 v_0 \sin \frac{\theta}{2}. \quad (2)$$

The observed maximum W_{80} value is found to be 498 and 410 km s^{-1} on the axis of the larger and smaller cone, respectively. Due to the limitation of our spatial resolution, we estimate the possible range of the opening angle to be $60^\circ \lesssim \theta \lesssim 90^\circ$, which introduces an $\sim 20\%$ uncertainty in the inferred v_0 . For $\theta = 70^\circ$, we attain an outflow velocity of $v_0 \simeq 520\text{--}630$ km s^{-1} .

If the observed W_{80} values are predominantly due to the projected velocities of the bulk motion of the outflow, the physical velocity of the outflowing gas must be high. The host galaxy, rotating at a speed of ~ 170 km s^{-1} (measured at 1–2 kpc from the center, see Section 4) close to that of the Milky Way (~ 220 km s^{-1} at the corresponding galactic radius, Bhattacharjee et al. 2014). This rotation speed indicates a host galaxy with comparable or slightly smaller mass than the Milky Way (although the rotation we observe may not reflect the large-scale dynamical mass of the system, and this is only a heuristic comparison). Considering that the Milky Way has an escape velocity of $550.9^{+32.4}_{-22.1}$ km s^{-1} (Kafle et al. 2014), the ionized gas traced by [O III] is probably (barely) escaping from the potential well of its host galaxy. However, we emphasize that in addition to the bulk flow, the local velocity distribution of the clouds in the outflow likely also contribute to the observed linewidth, resulting in a smaller outflow velocity.

Under the “Case B” assumption, the mass of the observed ionized gas is proportional to the product of $H\beta$ luminosity and electron density (Nesvadba et al. 2011;

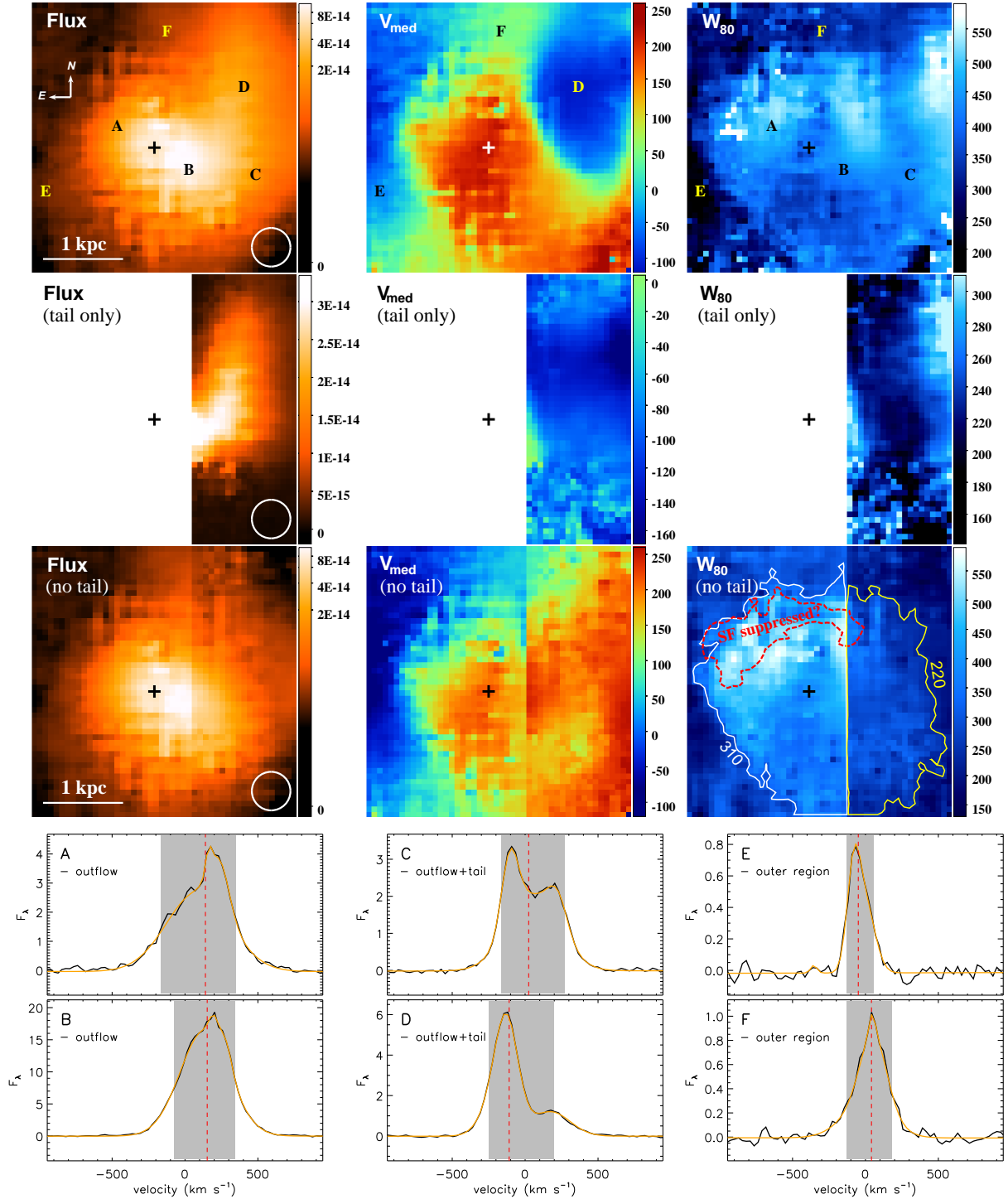


Figure 3. Mrk 509. **Top color maps:** The [O III] surface brightness (left column, in $\text{erg s}^{-1} \text{cm}^{-2} \text{\AA}^{-1}$, logarithmic scale except for the “tail”), median velocity (middle column, in km s^{-1}) and line width (W_{80} , right column, in km s^{-1}) maps. Our 2-Gaussian decomposition of the [O III] line allows for isolating the contribution from the “tail” structure (Figure 2) and a roughly spherical or elliptical structure likely due to an galactic outflow. Overlaid on the bottom right panel is the 220 km s^{-1} contour for the “tail” region and the 310 km s^{-1} contour for the rest of the FoV, which roughly depict the outflow structure. Red contour crudely marks where the narrow H β line is weakest (indicative of star formation suppression), which spatially coincides with the broadest [O III] line (see discussion in Section 5, cf. Figure 4). Central AGN is marked with a black cross, and the seeing at the observing site is shown by open circles. **Bottom spectra:** [O III] velocity profiles at 6 representative spatial positions (F_λ is in units of $10^{-17} \text{ erg s}^{-1} \text{cm}^{-2} \text{\AA}^{-1}$, within a $0.1''$ spatial pixel), including 2 outflow regions (“A”, “B”), 2 outflow plus “tail” regions (“C”, “D”), and 2 outer regions (“E”, “F”). The fitted line is in orange, the median velocity is marked by a red dashed line, and the velocity range enclosing W_{80} is a grey box.

Osterbrock & Ferland 2006; though this is actually a lower limit, see discussion in Liu et al. 2013b, Sec. 6). In this object, $H\beta$ follows the same spatial distribution as that of $[O\ III]$ because $[O\ III]/H\beta$ is a constant (Sec. 5.2.1; Fig. 5). Assuming that the electron density is distributed as $n_e = 10^3 (r/0.1\text{ kpc})^{-2} \text{ cm}^{-3}$ (Sec. 6.1.1), we infer that $\sim 60\%$ of the warm ionized gas is outflowing, therefore likely escaping from the galaxy’s potential well.

Absorption line analysis of the high quality HST COS spectrum reveal three kinematic components in this system, identified using the strong, unblended C IV and N V doublet lines. Their centroids are found at radial velocities of -38 , -156 and -220 km s^{-1} , respectively (Edmonds et al. 2011). These absorption outflow components are all at velocities smaller than the maximum line-of-sight velocity $v_0 \sin(\theta/2)$ of $300\text{--}360 \text{ km s}^{-1}$ (Equation 2) given by the bi-cone model built upon our IFU observations, implying crude consistency. The $\gtrsim 100 \text{ km s}^{-1}$ lower velocities in UV absorption are probably because these absorbers are far away from the primary biconical structure of the ionized gas outflow, indicating non-localized matter distribution and non-uniform velocity distributions beyond the scope of our simple model. These poorly understood uncertainties reflect the limitations of current knowledge on the physics of outflows, more realistic modeling and further observational scrutinization in the future are awaited to provide a handle.

5.2. Mrk 509

5.2.1. Spatial extent

In order to compare the distribution of AGN activity to that of newly formed stars, we decompose the $H\beta$ line into broad (FWHM = 2700 km s^{-1}) and narrow (FWHM = $140\text{--}640 \text{ km s}^{-1}$) components using 2-Gaussian fits, so that the emission from the broad line region and the narrow line region of the AGN is separated (note that $[O\ III]$ is emitted by the narrow line region only). The maps of signal-to-noise ratios at the peak of $[O\ III]$ and narrow $H\beta$ lines are shown in Figure 4, where the tidal tail feature has been removed, as described in Section 4. Faint $[O\ III]$ -emitting gas illuminated by massive stars are characterized by small linewidths (FWHM $\lesssim 200 \text{ km s}^{-1}$). Thus, the line intensity in those regions, scaling as the product of the linewidth and the peak flux, are thus more suppressed in $[O\ III]$ flux maps than in these signal-to-noise ratio maps. As a result, these maps are better for scrutinizing low surface brightness features than line intensity maps.

In figure 4, at least 5 $[O\ III]$ -emitting blobs surrounding the center are seen, which are distributed at a galactocentric distance of about 1.6 kpc . All these features are clearly seen in the narrow $H\beta$ signal-to-noise map at the same positions. In galactic environments, hydrogen recombination lines are emitted by interstellar gas ionized by young, massive stars with ages $\lesssim 10 \text{ Myr}$ (Liu et al. 2013c), rendering them reliable tracers of the current star formation rate (Kennicutt 1998; Liu et al. 2011) if dust extinction is carefully corrected for spatially-resolved studies (see discussion in Calzetti et al. 2007 and Liu et al. 2013d). Therefore, this spatial correspondence of $[O\ III]$ and narrow $H\beta$ implies significant contribution or even dominance of massive stars in producing

the warm ionized gas at this distance.

Furthermore, the ratio of these two maps reveal that $[O\ III]/H\beta_{\text{narrow}}$ is above 10 in the central $\sim 1 \text{ kpc}$ and decreases to 1–3 at a radius of 1.6 kpc and beyond (see Section 6.1 and Figure 5). In a BPT diagram (Baldwin et al. 1981), $[O\ III]/H\beta_{\text{narrow}} > 10$ implies AGN dominance, while $[O\ III]/H\beta_{\text{narrow}} \sim 1$ points to a low-ionization nuclear emission-line region (LINER, not applicable to this case) or star formation possibly mixed with AGN ionization. The combination of this fact and the spatial correspondence of $[O\ III]$ and narrow $H\beta$ features strongly indicate that the AGN’s dominating role in the interstellar radiation is taken over by star formation at a distance of $\sim 1\text{--}1.5 \text{ kpc}$. We therefore conclude that the full extent of predominating AGN ionization likely have been probed, in spite of our limited field of view ($3.3 \times 3.3 \text{ kpc}^2$).

An intriguing phenomenon is the indicative evidence for the outflow suppressing star formation: the weakest $H\beta$ (narrow) emission is found in an elongated region in the northeast to north direction from the center, at a radius a $\sim 1 \text{ kpc}$ (delineated with a cyan dashed curve in Figure 5); this region spatially coincides with where the line width W_{80} reaches its maximum (Figure 3). Similar evidence for outflows suppressing star formation activities has been reported in spatially resolved spectroscopy at $z = 2.4$ (Cano-Díaz et al. 2012). This further consolidates the conclusion in Liu et al. (2013b) that high line widths of $[O\ III]$ strongly implies outflowing gas.

The multi-wavelength campaign on Mrk 509 has derived a lower limit of $100\text{--}200 \text{ pc}$ for the outflow radius in this system Arav et al. (2012). This was inferred from the fact that the column densities of C IV and N V showed negligible variation between 2001 and 2009 despite a large change in ionizing flux, aided by Monte Carlo simulated light curves that statistically determined the distance limits. The galactocentric distance of 1.2 kpc that we determine from the features of a spherical outflow (Section 4) lies above these indirectly inferred lower limits comfortably.

5.2.2. Gas Kinematics

The extinction-free quasi-spherical outflow model proposed in Liu et al. (2013b) is applicable to Mrk 509, because of the round-ish morphology, the small velocity variation across the median velocity map, and the roughly flat radial profile of W_{80} within a radius of $\sim 1 \text{ kpc}$. Similar to the case of IRAS F04250–5718, we measure the outskirts of the ionized gas nebula (before reaching the star formation dominated region at $R \gtrsim 1.3 \text{ kpc}$), finding the best-fit power law of $[O\ III]$ surface brightness to be $I \propto R_{\parallel}^{-2.9 \pm 0.1}$. Changing Equation 1 to its original form in Liu et al. (2013b) (i.e. replacing R_{\parallel} and $v_0 \sin(\theta/2)$ with R and v_0 , respectively), we find for $\alpha = 3.9$,

$$W_{80} = 1.393 v_0.$$

To avoid additional uncertainties introduced by removing the linear tail structure, we only use the west (left) 60% part of the W_{80} map (Figure 3) where nonparametric measurements were performed on the original $[O\ III]$ line profile. The average W_{80} of the outflow in this region (defined by $W_{80} > 310 \text{ km s}^{-1}$) is $410 \pm 72 \text{ km s}^{-1}$,

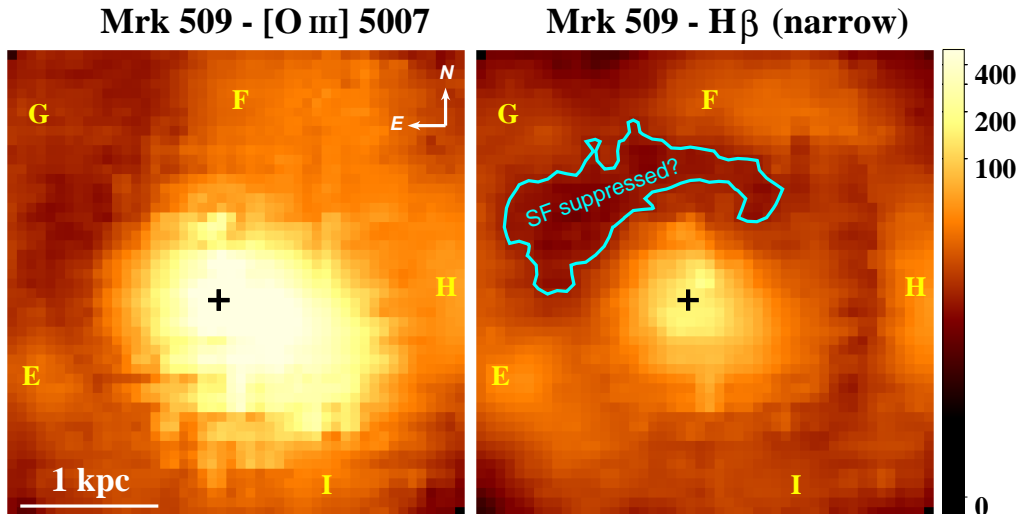


Figure 4. Maps of signal-to-noise ratios measured at the peak of $[\text{O III}] 5007\text{\AA}$ and the narrow $\text{H}\beta$ emission line profiles. These maps allow for seeing low surface brightness features in the outer region more easily than previous flux maps (Figure 3, left panels). At least 5 $[\text{O III}]$ -emitting blobs surrounding the center are seen in both panels (marked “E” to “I”). Note that the spectra at “E” and “F” have been shown in Figure 3. The cyan contour depicts the region of the weakest narrow $\text{H}\beta$ emission, which spatially coincides with where W_{80} reaches its maximum values, indicative of star formation being suppressed by the outflow (cf. Figure 3, W_{80} maps).

translating to a physical outflow velocity of $v_0 = 293 \pm 51 \text{ km s}^{-1}$, where the standard deviations are reported as uncertainties. W_{80} reaches its maximum $\sim 510 \text{ km s}^{-1}$ in the northeast of the AGN, thus the largest possible outflow velocity is $v_0 \sim 370 \text{ km s}^{-1}$.

Since this outflow is quasi-spherical, velocities from absorption line analyses can be directly compared to our model (projection effects are minimized). Nine independent outflow components have been identified from the N V , Si IV and C IV troughs by Arav et al. (2012). The strongest absorption feature emerges at $\sim -320 \text{ km s}^{-1}$, in agreement with our best estimate $v_0 = 293 \pm 51 \text{ km s}^{-1}$. The highest velocity measured in that work (425 km s^{-1}) slightly exceeds the upper bound we derive here (370 km s^{-1}), but the corresponding component is relatively weak. Moreover, as discussed in Section 5.1.2, absorption line analyses intrinsically have significantly higher spatial resolution and are more sensitive to the local velocity distribution of the clouds residing on our line of sight, which is likely smeared out in the IFU data which may only detect the bulk flow. Besides the uncertainty of our simplistic model, this difference could also be responsible for the small discrepancy (several tens of km s^{-1}). As a result, these two independent and complementary investigations provide consistent results.

5.3. Electron density

Our IFU spectra include the conventional electron density (n_e) diagnostic, $[\text{S II}] \lambda\lambda 6717, 6731\text{\AA}$, facilitating a comparison of n_e to our previous absorption line analyses. To do this, we fit the $[\text{S II}]$ doublet simultaneously using the same line width and velocity structure to derive a $[\text{S II}] 6731\text{\AA}/6717\text{\AA}$ ratio map.

The theoretical dependence of this line ratio on n_e is then calculated using Version 7.1 of CHIANTI, an atomic database for spectroscopic diagnostics of astrophysical plasmas (Dere et al. 1997; Landi et al. 2013). In this calculation, we assume a typical temperature of warm ionized gaseous nebulae that produce narrow emission lines, $T = 10^4 \text{ K}$ (but note n_e is only weakly dependent on the

assumed temperature as $\propto T^{-1/2}$, Osterbrock & Ferland 2006).

As a result, we find $n_e = 1300 \pm 140 \text{ cm}^{-3}$ and $1200 \pm 110 \text{ cm}^{-3}$ in the center of IRAS F04250–5718 and Mrk 509, respectively. We limit our n_e measurement to locations where the $[\text{S II}]$ doublet has a signal-to-noise ratio of at least 3. At the maximum radii set by the above requirement, we find $n_e < 100 \text{ cm}^{-3}$ at 1 kpc away from the center of Mrk 509, and $n_e < 200 \text{ cm}^{-3}$ at 2 kpc from the center of IRAS F04250–5718 (these values are upper limits because n_e already reaches the lower critical density for deexcitation, where the line ratio is no longer sensitive to n_e). In Section 6.1, n_e at the break radius is necessary for deriving the energetics of these outflows, which is, unfortunately, not measurable from our data, but the adopted value of 10 cm^{-3} is consistent with these limits.

In the absorption outflow of IRAS F04250–5718, a 3σ upper limit of $n_e < 30 \text{ cm}^{-3}$ is derived from the constraint on the $\text{C II}^*/\text{C II}$ ratio placed by the non-detection of C II^* (Edmonds et al. 2011). These absorbers are found to be located at $\sim 3 \text{ kpc}$ from the center; at this distance, we derive a consistent upper limit from $[\text{S II}]$ emission lines, $n_e < 200 \text{ cm}^{-3}$.

UV absorption lines allowed Arav et al. (2012) to measure electron density for outflow components T1 and T2 in Mrk 509, $n_e = 10^{3.0-3.7}$ and $10^{2.9-3.1} \text{ cm}^{-3}$, respectively, but the distance for the absorbers is only constrained to be $> 200 \text{ pc}$. At these distances, the $[\text{S II}]$ emission lines in our data give $n_e < 900 \text{ cm}^{-3}$, a result in broad agreement with Arav et al. (2012), given the $\sim 10\%$ uncertainty.

6. DISCUSSION

6.1. Outflow energetics

In a possibly realistic physical picture, numerous relatively dense clouds filling only a fraction of the volume as low as $\lesssim 1\%$, which are embedded in a rarefied hot wind which might even dominate the mass and energy of galactic outflows. At small galactic radii, the sur-

face of these clouds are ionized by the central AGN and emits the observed narrow lines (“ionization-bounded”). As the wind carries these clouds to larger radii, the decreasing pressure allow them to expand and gradually become optically-thin, and finally fully ionized at a certain distance, entering the “matter-bounded regime” (cf. discussion in Liu et al. 2013b).

This hypothesis of transition is supported by a series of recent observations (Liu et al. 2013a, 2014; Hainline et al. 2013, 2014), of which the most direct is the radial profile of [O III]-to- $H\beta_{\text{narrow}}$ persisting at $\gtrsim 10$ at small radii that starts to decline at a break radius of $R_{\text{br}} = 4\text{--}11$ kpc, beyond which $\text{He II}/H\beta$ increases (Liu et al. 2013a). This newly found phenomenon has enabled Liu et al. (2013b) to constrain the estimation of the mass flow rate (\dot{M}) and kinetic luminosity (\dot{E}_{kin}) of the outflows significantly better than previous studies. In this section, we follow that work to constrain the energetics of the two objects.

6.1.1. Energetics: Mrk 509

The above [O III]/ $H\beta$ behavior is also seen in Mrk 509, where the break radius is $R_{\text{br}} \simeq 1.1$ kpc (Figure 5). At this radius, we measure the $H\beta$ surface brightness to be $\Sigma_{H\beta} = 2.6 \times 10^{-16} \text{ erg s}^{-1} \text{ cm}^{-2} \text{ arcsec}^{-2}$ after correcting the cosmological dimming effect by a factor of $(1+z)^4$. This observation facilitates direct application of the reasoning in Liu et al. (2013b).

The electron density in outflows is poorly known. In more luminous and energetic objects at higher redshifts, Greene et al. (2011) find $\sim 100 \text{ cm}^{-3}$ in radio-quiet quasar nebulae, while Nesvadba et al. (2006, 2008) find a few 100 cm^{-3} in powerful radio galaxies. These results are not dissimilar to the density in the sub-kpc neighborhood of our AGNs (Section 5.3). The observed [O III] surface brightness profile, scaling as R^{-3} in both our objects (Section 5.1.2 and Section 5.2.2), is a natural consequence of $n_e \propto r^{-2}$ (Liu et al. 2013a). In both objects, the [S II] emission lines give $n_e \sim 1000 \text{ cm}^{-3}$ at a galactocentric radius of 0.1 kpc; it will fall to $\sim 10 \text{ cm}^{-3}$ at the break radius (1.1 kpc for Mrk 509). Although we can only measure an upper limit at ~ 1 kpc ($n_e < 100 \text{ cm}^{-3}$; Section 5.3), this extrapolation leads to n_e similar to Rupke & Veilleux (2013); those authors assume $n_e = 10 \text{ cm}^{-3}$ based on measurements of the superbubble in NGC 3079 ($n_e = 5\text{--}100 \text{ cm}^{-3}$; Veilleux et al. 1994; Cecil et al. 2001). The above considerations lead us to adopt $n_e = 10 \text{ cm}^{-3}$ for the following calculations.

We find the $H\beta$ line emission to fall off as $\Sigma_{H\beta} \propto R^{-2.1}$ in this object, changing the numerical factor 1.44 in Equation 18 in Liu et al. 2013b to 1.94. Using Equation 22 therein, we estimate the mass flow rate to be

$$\frac{\dot{M}}{5.2 \text{ M}_{\odot} \text{ yr}^{-1}} = \frac{\Sigma_{H\beta}(R_{\text{br}})}{2.6 \times 10^{-16} \text{ erg s}^{-1} \text{ cm}^{-2} \text{ arcsec}^{-2}} \times \frac{R_{\text{br}}}{1.1 \text{ kpc}} \frac{v_0}{293 \text{ km s}^{-1}} \left(\frac{n_e}{10 \text{ cm}^{-3}} \right)^{-1}, \quad (3)$$

which is normalized by our derived outflow velocity, 293 km s^{-1} (Section 5). As a consequence, the kinetic lumi-

nosity of the outflow, $\dot{E}_{\text{kin}} = \dot{M} v_0^2 / 2$, is given by

$$\frac{\dot{E}_{\text{kin}}}{1.4 \times 10^{41} \text{ erg s}^{-1}} = \frac{\dot{M}}{5.2 \text{ M}_{\odot} \text{ yr}^{-1}} \left(\frac{v_0}{293 \text{ km s}^{-1}} \right)^2. \quad (4)$$

The momentum flow rate is $\dot{P} = \dot{M} v = 9.6 \times 10^{33} \text{ dyne}$, or $\log(c\dot{P}/L_{\odot}) = 10.9$, similar to that of the outflows driven by low-redshift major mergers (Rupke & Veilleux (2013) find a range of 10.0–12.8).

The uncertainty of these results is largely caused by the poorly constrained n_e . \dot{M} and \dot{E}_{kin} for other electron densities can be easily calculated using the n_e^{-1} dependence (Equations 3 and 4). The conservative constraint that [O III]-emitting clouds only fill a fraction of the volume results in a lower limit of $n_e \sim 0.1 \text{ cm}^{-3}$ (Equation 21 in Liu et al. 2013b). Along with the measured upper limit, $n_e < 100 \text{ cm}^{-3}$ (Section 5.3), we find firm lower limits using Equations 3 and 4,

$$0.5 \text{ M}_{\odot} \text{ yr}^{-1} < \dot{M} < 520 \text{ M}_{\odot} \text{ yr}^{-1},$$

$$1.4 \times 10^{40} \text{ erg s}^{-1} < \dot{E}_{\text{kin}} < 1.4 \times 10^{43} \text{ erg s}^{-1}.$$

Hence, we conclude that Mrk 509 is driving an outflow with $\dot{M} \sim 5 \text{ M}_{\odot} \text{ yr}^{-1}$ and $\dot{E} \sim 1 \times 10^{41} \text{ erg s}^{-1}$, with an upper (lower) limit of 100 (10) times larger (smaller) for both quantities. The ratio of the momentum flux of the outflow to the AGN radiation is $\dot{P}/(L_{\text{bol}}/c) \sim 0.3$. The outflow kinetic luminosity is only $\sim 0.01\%$ of the bolometric luminosity of Mrk 509, and $\sim 0.002\%$ of its Eddington luminosity ($L_{\text{bol}} = 1 \times 10^{45} \text{ erg s}^{-1}$, $L_{\text{bol}}/L_{\text{Edd}} \simeq 0.16$; Kaspi et al. 2000). Since theoretical modeling predicts that significant feedback requires $\gtrsim 0.5\text{--}5\%$ of the AGNs luminosity to be converted to the mechanical energy of the outflow (e.g. Di Matteo et al. 2005; Hopkins & Elvis 2010), the outflow in Mrk 509 does not produce feedback strongly affecting the evolution of the host galaxy.

On the absorption line front, Arav et al. (2012) find an average hydrogen column density of $N_{\text{H}} = 10^{19.8} \text{ cm}^{-2}$ and a velocity of $\sim 300 \text{ km s}^{-1}$ in the outflow of Mrk 509. Adopting a solid angle of 4π for the quasi-sphere geometry and an outflow radius of 1.2 kpc obtained in this work, we find $\dot{M} = 3.3 \text{ M}_{\odot} \text{ yr}^{-1}$ (Equation 7, Edmonds et al. 2011), and $\dot{E}_{\text{kin}} = \dot{M} v^2 / 2 = 9.3 \times 10^{40} \text{ erg s}^{-1}$, in agreement with the above determination within a factor of 1.6.

6.1.2. Energetics: IRAS F04250–5718

The uniform [O III]-to- $H\beta_{\text{narrow}}$ ratio $\gtrsim 10$ across the whole map implies a break radius beyond the largest radius reached by our field of view ($R_{\text{br}} \gtrsim 5.5$ kpc, see Figure 5). However, the largest break radius that has ever been observed is 11 kpc, seen in SDSS J032144.11+001638.2 at $z = 0.643$ (Liu et al. 2013a), one of the most luminous quasars at that redshift, with a bolometric luminosity of $\gtrsim 10^{46.5} \text{ erg s}^{-1}$. IRAS F04250–5718 is expected to have $R_{\text{br}} \lesssim 10$ kpc due to its lower luminosity ($L_{\text{bol}} \sim 9 \times 10^{45} \text{ erg s}^{-1}$, Edmonds et al. 2011).

At the 5.5 kpc radius, the [O III] surface brightness is measured to be $1.3 \times 10^{-15} \text{ erg s}^{-1} \text{ cm}^{-2} \text{ arcsec}^{-2}$ after correcting for the cosmological dimming effect, thus

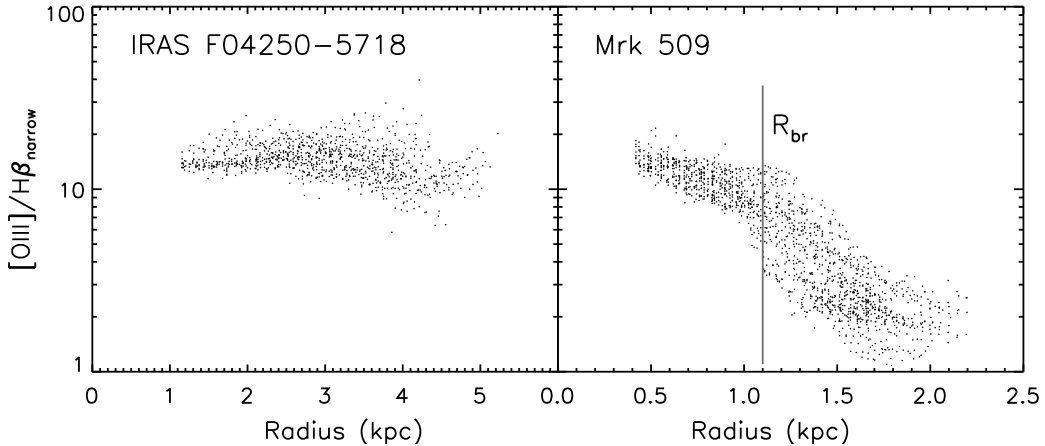


Figure 5. The radial profile of the intensity ratio of [O III]5007 to the narrow component of H β (obtained from 2-Gaussian decomposition) for IRAS F04250–5718 and Mrk 509. The ratio persists at a constant level (~ 10) in the whole field of view for the former, but starts to decline rapidly at a “break” radius of 1.1 kpc for the latter (a prevalent phenomenon discovered in $z \sim 0.5$ luminous quasars by Liu et al. 2013a). This radius (marked with a vertical line) implies a transition of the gaseous nebulae from an ionization-bounded regime to a matter-bounded regime, and facilitates our calculation of the kinetic luminosity and the mass flow rate of the outflows.

the surface brightness profile $\Sigma_{[\text{O III}]} \propto R^{-3.0 \pm 0.1}$ (Section 5.1.2) predicts $\Sigma_{[\text{O III}]}(11 \text{ kpc}) = 1.7 \times 10^{-16} \text{ erg s}^{-1} \text{ cm}^{-2} \text{ arcsec}^{-2}$, and thus $\Sigma_{\text{H}\beta}(11 \text{ kpc}) \gtrsim 0.1 \Sigma_{[\text{O III}]} = 1.7 \times 10^{-17} \text{ erg s}^{-1} \text{ cm}^{-2} \text{ arcsec}^{-2}$.

Compared to a spherically symmetric geometry, the bi-conical configuration of the outflow introduces a correction factor of $1 - \cos(\theta/2)$, where $\theta \simeq 70^\circ$ is the opening angle of each cone (Section 4). Now that both $\Sigma_{[\text{O III}]}$ and $\Sigma_{\text{H}\beta}$ fall off as R^{-3} , the numerical factor 1.44 in Equation (18) in Liu et al. (2013b) increases to 1.57. For an outflow velocity of 520 km s^{-1} (the lower bound, Section 5.1.2), assuming $R_{\text{br}} = 11 \text{ kpc}$ and $n_e = 10 \text{ cm}^{-3}$, Equation 3 gives

$$\dot{M} > 1.3 M_\odot \text{ yr}^{-1},$$

$$\dot{P} > 4.3 \times 10^{33} \text{ dyne}, \quad \dot{E}_{\text{kin}} > 1.2 \times 10^{41} \text{ erg s}^{-1}.$$

As discussed in Section 6.1.1, compared to Mrk 509, this object has similar n_e in the center and similar n_e radial profile, but its break radius is larger by a factor of a few or more, and n_e at the break radius is likely lower than 10 cm^{-3} . However, only an upper limit, $n_e < 200 \text{ cm}^{-3} \text{ s}^{-1}$, can be derived from our data, after all. Here we adopt $n_e = 10 \text{ cm}^{-3}$ for consistency (which pushes the above results to their lower limits, see below).

Since the actual electron density is likely lower, and the smallest possible $\Sigma_{\text{H}\beta}$ is used here; although R_{br} may have been overestimate by a factor of ≤ 2 , the overly large break radius leads to an underestimate of the steep declining $\Sigma_{\text{H}\beta}$ (by a factor of ≤ 8) that itself cannot balance out. For the above reasons, Equation 6.1.2 gives lower limits of the outflow energetics.

On the other hand, adopting $n_e = 0.1 \text{ cm}^{-3}$, $R_{\text{br}} = 5.5 \text{ kpc}$ and $v_0 = 630 \text{ km s}^{-1}$ (upper bound) sets conservative upper limits

$$\dot{M} < 690 M_\odot \text{ yr}^{-1},$$

$$\dot{P} < 2.7 \times 10^{36} \text{ dyne}, \quad \dot{E}_{\text{kin}} < 8.6 \times 10^{43} \text{ erg s}^{-1}.$$

The ratio of the momentum flux of the outflow to the AGN radiation is only loosely constrained to

$\dot{P}/(L_{\text{bol}}/c) = 0.01\text{--}9$. The kinetic luminosity of the outflow in this system is insignificant, being only $\gtrsim 0.002\%$ of its bolometric luminosity ($\sim 9 \times 10^{45} \text{ erg s}^{-1}$, Edmonds et al. 2011). Therefore, the outflow in IRAS F04250–5718 is not a significant feedback agent, similar to the case of Mrk 509.

Edmonds et al. (2011) find a velocity of 220 km s^{-1} and a column density lower limit of $N_{\text{H}} > 10^{19.55} \text{ cm}^{-2}$ in the absorption outflow of this object. Adopting an outflow radius of 3 kpc, a solid angle of $\Omega/4\pi = 0.2$ derived from our IFU data and deprojecting their velocities using $\theta = 70^\circ$ (the outflow lies approximately in the plane of the sky, Section 6.1.2), their results lead to $\dot{M} \sim 1.2 M_\odot \text{ yr}^{-1}$, and $\dot{E}_{\text{kin}} \sim 5.5 \times 10^{40} \text{ erg s}^{-1}$, in agreement with the above determination within a factor of ~ 2 .

6.2. More on Mrk 509’s structure

Recent long-slit (Fischer et al. 2013) and IFU spectroscopy (Fischer et al. 2015) demonstrate that Mrk 509 is likely a minor merger system, where gas is inflowing and fueling the central AGN through the linear tidal tail and the “southwestern jut” (cf. Figure 2). In this section, we discuss in detail the dynamical structure of this system by combining and comparing our data to previous observations.

The host galaxy is nearly face-on ($i = 36.4^\circ$ as per the HyperLeda database⁴, Paturel et al. 2003; Yaqoob et al. 2003 find $i = 41^\circ$), and the linear tidal tail is likely located in front of the disk, as otherwise it would have been severely extinguished by dust and become invisible. (To test this judgement, we isolate the tidal tail’s emission in the H α and H β lines using 3-Gaussian fits accounting for the broad base and the double-peak structure, and find the average H α /H β ratio on the tail to be 2.8 ± 0.5 . Under “Case B” assumption, the intrinsic line ratio is 2.7–3.0 for a wide range of temperature and electron density ($T = 5000\text{--}30000 \text{ K}$, $n_e = 10^2\text{--}10^6 \text{ cm}^{-3}$). Hence, the observed line ratio is consistent with negligible dust extinction, confirming our conclusion that the galactic disk

⁴ <http://leda.univ-lyon1.fr>

is behind the tidal tail.) Therefore, in case the “southwestern jut” is physically connected to the tail and serves as a tunnel for inflowing gas, we expect to see velocity smoothly transition from $\sim -100 \text{ km s}^{-1}$ to zero then to positive velocities, along the route of the tail, then the “jut”, finally the AGN neighborhood.

Nevertheless, in our data we find that the “jut” and the long linear tail, although appear to be connected, have distinct velocities everywhere (different by $200\text{--}350 \text{ km s}^{-1}$). Furthermore, the [O III] intensity map of the tidal tail (Figure 3), middle row) shows that it likely switches direction sharply (southward to eastward) to approach the nucleus before it reaches the main body of the “jut”, at only $\sim 0.4''$ (R.A. distance) south of the AGN. This phenomenon is confirmed by IFU maps with higher spatial resolution Fischer et al. (2015). Hence, we conclude that the linear tail and the “jut” are physically unrelated, but are superposed by projection effects; the gas in the linear tail is likely indeed inflowing (Fischer et al. 2013), but it may use its own route instead of inflowing through the “southwestern jut”.

However, with the linear tidal tail removed using 2-Gaussian fits, interpreting the remaining structures (including the “jut”) is still nontrivial. Fischer et al. (2015) performed IFU spectroscopy assisted by adaptive optics in the [S III] $0.95 \mu\text{m}$ emission line. In their data with higher ($\sim 0.1''$) angular resolution, they observe a $\sim 2''$ elliptical region (schematically shown by an ellipse in Figure 6) in their smaller FoV ($3'' \times 3''$). This region shows a well defined velocity gradient (upper left panel of Figure 4 in their paper), allowing them to fit the velocity field to a rotating disk model.

However, this rotation pattern is not seen in our median velocity maps (Figure 3): we do observe negative velocities close to the east edge of the FoV, but we see a roughly constant velocity across a large round-ish region when the tail is removed, which is deemed as indicative evidence for a quasi-spherical outflow in Section 4.2.

This seeming discrepancy is, in fact, due to the higher signal-to-noise ratios of our data. In fact, if we determine the velocity field from the peak wavelength of the [O III] line instead of calculating the median velocity, the pattern seen by Fischer et al. (2015) is reproduced with accuracy. As shown in Figure 6, the rotation axis of their best-fit model (dashed line) is consistent with our zero-velocity spatial pixels (here we force the velocity at the center to be zero for comparison purposes). Obviously the rotation pattern is actually not restricted within a circumnuclear disk ($\sim 0.7 \text{ kpc}$ in radius) as Fischer et al. (2015) find, but exists on a scale as wide as $3.3 \times 3.3 \text{ kpc}^2$ (our whole FoV) or larger. This finding may alleviate the issue of the rather high rotation speed those authors derived ($\sim 500 \text{ km s}^{-1}$), if their model fits are performed on an area larger by a factor of ~ 5 .

In Fischer et al. (2015), [S III] is detected with $S/N < 3$ in $\sim 40\%$ area of the FoV (roughly between the ellipse and the box in Figure 6), where we detect [O III] 5007\AA line with $S/N > 15$ in every spaxel (Figure 4). In low S/N data, the weak broad base of an emission line, which may contain outflow signatures, can be easily submerged into noise, so that a single Gaussian is sufficient for line fitting (this effect has been simulated and discussed in Liu et al. (2013b, Section 3.4). This difference explains

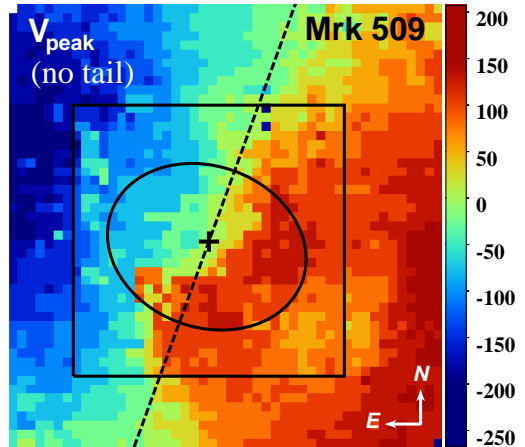


Figure 6. [O III] 5007\AA emission line’s peak velocity map of Mrk 509 (in km s^{-1} ; the velocity at the AGN position is set to be zero). In contrast to the median velocity map (more sensitive to the broad base of the line profile, Figure 3) that shows a roundish structure in the center likely caused by an outflow, this map exhibits a well defined large-scale rotation pattern. Fischer et al. (2015) find a similar rotating pattern in the [S III] $0.95 \mu\text{m}$ emission line, with an axis (dashed line) in consistency with this map; those authors attribute this motion to a rotating disk $\sim 2''$ in diameter (schematically shown as an ellipse) in the center of their $3'' \times 3''$ FoV (box), but we see the rotation taking place on a larger scale, co-existing with a quasi-spherical or wide-angle outflow. However, the uncertainties that the rotating gas introduces into our outflow modeling are insignificant (see Section 6.2).

why in majority of their spaxels [S III] can be fitted with a single Gaussian profile, which only happens in a few percent of the spaxels in our [O III] analysis. It also results in our velocity map different from the one obtained by Fischer et al. (2015), as median velocity is more sensitive to the broad base than fits to lower S/N data, and thus likely traces outflow kinematics better.

Meanwhile, Fischer et al. (2015) also detect a second Gaussian component northeast to the AGN, which they suspect is an inflow or outflow. We now obtain supportive evidence for an outflow — this region spatially coincides with where [O III] is broadest and where the narrow $H\beta$ is weakest (Figures 3 and 5), indicating star formation being suppressed by an outflow. This northeast outflow region shows an opening angle of $\sim 90^\circ$ in the data of Fischer et al. (2015), whereas our data points to a significantly wider angle or even a spherical morphology (Section 4.2).

The above considerations lead us to conclude that a wide-angle outflow and a large-scale rotating gas likely both contribute to the kinematics (beside the inflowing tidal tail in the west). Decomposing the two components is difficult, either spatially or spectroscopically, but we reckon that the contribution from the rotating gas is not significant. Empirically, rotating gas in the host galaxy produces emission lines narrower than those from outflows ($W_{80} \lesssim 200 \text{ km s}^{-1}$ vs. $W_{80} \gtrsim 300\text{--}400 \text{ km s}^{-1}$). Therefore, in general, W_{80} directly measured from the observed line profile is not significantly different from the line width of the outflow only (unless the outflow is remarkably fainter than the rotating gas, in which case the measured W_{80} provides a lower limit). This assertion is supported by the existing data: Fischer et al. (2015) separate out the outflow contribution using two-Gaussian fits and finding the outflow component in the northeast region to have $W_{80} = 500\text{--}600 \text{ km s}^{-1}$, in agreement

with our direct measurement from the observed [O III] line (Figure 3). Hence, the line width used for calculating the outflow velocity in Section 4.2 is confirmed by an independent observation, and the contamination from the rotating galactic gas is trivial.

Thus far, we have assumed a spherical geometry for the outflow in Mrk 509. As discussed above, the north-east quadrant is where the existence of an outflow is supported by the strongest evidence. Since the firm lower limit of its opening angle is $\sim 90^\circ$ as given by (Fischer et al. 2015), assuming such a biconical geometry with its axis close to the plane of the sky leads to a velocity larger by $\sim \sqrt{2}$ and an additional filling factor of ~ 0.3 , and thus a mass flow rate and a kinetic luminosity not dissimilar (within a factor of ~ 2) to the results of assuming a spherical symmetry.

7. SUMMARY

This work is the first effort to bridge integral field spectroscopy and absorption line analysis investigations on the ionized phase of AGN outflows, the two independent and complementary approaches to determine outflow properties. We present Gemini IFU observations of the ionized gas nebulae around two low-luminosity quasars, Mrk 509 and IRAS F04250–5718. The outflow distances from the central AGNs have been indirectly determined from UV absorption line analyses, which are directly tested by our IFU observations in this work.

We demonstrate that IRAS F04250–5718 shows a clear case where a biconical outflow extending out to at least 2.9 kpc from the center, in agreement with the result of absorption line analysis ($R \gtrsim 3$ kpc). The opening angle of each cone is $\sim 70^\circ$, and the outflow axis is $\sim 20^\circ$ away from the axis of the galactic disk rotating at a speed of ~ 170 km s $^{-1}$. The outflowing gas, with a derived physical velocity of 580 ± 80 km s $^{-1}$, is probably (barely) escaping from the potential well of its host galaxy. We obtain lower limits of the mass flow rate, $\dot{M} > 1.3 M_\odot$ yr $^{-1}$, the momentum flux rate $\dot{P} > 4.3 \times 10^{33}$ dyne, and the kinetic luminosity $\dot{E}_{\text{kin}} > 1.2 \times 10^{41}$ erg s $^{-1}$.

Mrk 509 is a more complicated system especially because of a linear tidal tail. After removing the tidal tail spectroscopically, we find a quasi-spherical outflow with a radius of ~ 1.2 kpc, also consistent with pre-existing absorption line analysis (a lower limit of 100–200 pc). The spatial coincidence of the highest [O III] line widths and the weakest narrow H β emission is indicative evidence for the outflow suppressing the formation of stars. Using the derived outflow velocity of 290 ± 50 km s $^{-1}$, we estimate a mass flow rate of $\dot{M} \sim 5.2 M_\odot$ yr $^{-1}$, a momentum flux rate of $\dot{P} \sim 9.6 \times 10^{33}$ dyne, and a kinetic luminosity of $\dot{E}_{\text{kin}} \sim 1.4 \times 10^{41}$ erg s $^{-1}$.

Adopting the outflow radii and geometric parameters measured from IFU, absorption line analyses would yield mass flow rates and kinetic luminosities that are in agreement with our IFU determination within a factor of ~ 2 . Measuring the outflow properties is challenging, and the multiple difficulties lead to relatively large uncertainties. However, we emphasize that the lower and upper limits we derived in this work spanning wide ranges are rather (maybe even overly) conservative, and should be understood as firm limits instead of limits with statistical meanings (e.g. 3σ limits). The measured values of

the outflow rates and energetics are reasonably reliable, and the above agreement between IFU and absorption line analyses is a justified validation.

The [S II] $\lambda\lambda 6717, 6730$ Å doublet allows us to derive electron densities in the central 1–2 kpc of both objects. The derived electron densities are in agreement with the previously inferred values from their absorption outflows (Mrk 509: $n_e \sim 10^3$ cm $^{-3}$ at ~ 100 pc from the center; IRAS F04250–5718: $n_e < 200$ cm $^{-3}$ at $\gtrsim 2$ kpc).

We conclude that both the spatial locations and the kinematics of these outflows determined from IFU spectroscopy of emission lines are consistent with those derived from previous UV absorption line analyses. Theoretical modeling predicts that significant feedback requires ~ 0.5 –5% of the AGN’s Eddington luminosity to be converted to the mechanical energy of the outflow. Feedback in these systems is taking place on kpc or galaxy-wide scales, but is inadequate for regulating the evolution of their galaxy hosts effectively (kinetic luminosity is only $\gtrsim 0.002$ –0.01% of the bolometric luminosity), unless it used to be significantly more energetic in the past.

We thank Gerard A. Kriss and Steven B. Kraemer for helpful discussions. We are grateful to the anonymous referee for a careful reading of the manuscript. G.L. and N.A. acknowledge support from NSF grant AST 1413319 as well as NASA STScI grants GO 11686 and GO 12022. D.S.N.R. was supported by a Cottrell College Science Award from the Research Corporation for Science Advancement.

Based on observations obtained at the Gemini Observatory (acquired through the Gemini Science Archive and processed using the Gemini IRAF package, Program ID: GS-2013B-Q-84), which is operated by the Association of Universities for Research in Astronomy, Inc., under a cooperative agreement with the NSF on behalf of the Gemini partnership: the National Science Foundation (United States), the National Research Council (Canada), CONICYT (Chile), the Australian Research Council (Australia), Ministério da Ciência, Tecnologia e Inovação (Brazil) and Ministerio de Ciencia, Tecnología e Innovación Productiva (Argentina).

This research has made use of the NASA/IPAC Extragalactic Database (NED) which is operated by the Jet Propulsion Laboratory, California Institute of Technology, under contract with the National Aeronautics and Space Administration. We acknowledge the usage of the HyperLeda database (<http://leda.univ-lyon1.fr>). CHIANTI is a collaborative project involving George Mason University, the University of Michigan (USA) and the University of Cambridge (UK).

Facilities: Gemini-South (GMOS).

REFERENCES

- Alexander, D. M., Swinbank, A. M., Smail, I., McDermid, R., & Nesvadba, N. P. H. 2010, MNRAS, 402, 2211
- Aoki, K., Oyabu, S., Dunn, J. P., et al. 2011, PASJ, 63, 457
- Arav, N., Borguet, B., Chamberlain, C., Edmonds, D., & Danforth, C. 2013, MNRAS, 436, 3286
- Arav, N., Edmonds, D., Borguet, B., et al. 2012, A&A, 544, AA33
- Baldwin, J. A., Phillips, M. M., & Terlevich, R. 1981, PASP, 93, 5
- Bautista, M. A., Dunn, J. P., Arav, N., et al. 2010, ApJ, 713, 25

- Bhattacharjee, P., Chaudhury, S., & Kundu, S. 2014, *ApJ*, 785, 63
- Borguet, B., Hutsemékers, D., Letawe, G., Letawe, Y., & Magain, P. 2008, *A&A*, 478, 321
- Borguet, B. C. J., Edmonds, D., Arav, N., Dunn, J., & Kriss, G. A. 2012a, *ApJ*, 751, 107
- Borguet, B. C. J., Edmonds, D., Arav, N., Benn, C., & Chamberlain, C. 2012, *ApJ*, 758, 69
- Borguet, B. C. J., Arav, N., Edmonds, D., Chamberlain, C., & Benn, C. 2013, *ApJ*, 762, 49
- Boroson, T. A., & Green, R. F. 1992, *ApJS*, 80, 109
- Calzetti, D., Kennicutt, R. C., Engelbracht, C. W., et al. 2007, *ApJ*, 666, 870
- Cano-Díaz, M., Maiolino, R., Marconi, A., et al. 2012, *A&A*, 537, LL8
- Carone, T. E., Peterson, B. M., Bechtold, J., et al. 1996, *ApJ*, 471, 737
- Cecil, G., Bland-Hawthorn, J., Veilleux, S., & Filippenko, A. V. 2001, *ApJ*, 555, 338
- Chamberlain, C., Arav, N., & Benn, C. 2015, *MNRAS*, submitted
- Choi, E., Naab, T., Ostriker, J. P., Johansson, P. H., & Moster, B. P. 2014, *MNRAS*, 442, 440
- Ciotti, L., Ostriker, J. P., & Proga, D. 2010, *ApJ*, 717, 708
- Cresci, G., Mainieri, V., Brusa, M., et al. 2015, *ApJ*, 799, 82
- Crenshaw, D. M., Kraemer, S. B., Hutchings, J. B., et al. 2000, *AJ*, 120, 1731
- Dai, X., Shankar, F., & Sivakoff, G. R. 2008, *ApJ*, 672, 108
- Davies, R. L., Schirmer, M., & Turner, J. E. H. 2015, *MNRAS*, 449, 1731
- de Kool, M., Arav, N., Becker, R. H., et al. 2001, *ApJ*, 548, 609
- de Kool, M., Becker, R. H., Gregg, M. D., White, R. L., & Arav, N. 2002, *ApJ*, 567, 58
- de Kool, M., Korista, K. T., & Arav, N. 2002, *ApJ*, 580, 54
- Dere, K. P., Landi, E., Mason, H. E., Monsignor Fossi, B. C., & Young, P. R. 1997, *A&AS*, 125, 149
- Di Matteo, T., Springel, V., & Hernquist, L. 2005, *Nature*, 433, 604
- Dunn, J. P., Bautista, M., Arav, N., et al. 2010, *ApJ*, 709, 611
- Edmonds, D., Borguet, B., Arav, N., et al. 2011, *ApJ*, 739, 7
- Faucher-Giguère, C.-A., Quataert, E., & Murray, N. 2012, *MNRAS*, 420, 1347
- Fischer, T. C., Crenshaw, D. M., Kraemer, S. B., & Schmitt, H. R. 2013, *ApJS*, 209, 1
- Fischer, T. C., Crenshaw, D. M., Kraemer, S. B., et al. 2015, *ApJ*, 799, 234
- Fu, H., & Stockton, A. 2009, *ApJ*, 690, 953
- Gabel, J. R., Kraemer, S. B., Crenshaw, D. M., et al. 2005, *ApJ*, 631, 741
- Ganguly, R., & Brotherton, M. S. 2008, *ApJ*, 672, 102
- Greene, J. E., Zakamska, N. L., Ho, L. C., & Barth, A. J. 2011, *ApJ*, 732, 9
- Guainazzi, M., Comastri, A., Stirpe, G. M., et al. 1998, *A&A*, 339, 327
- Hainline, K. N., Hickox, R., Greene, J. E., Myers, A. D., & Zakamska, N. L. 2013, *ApJ*, 774, 145
- Hainline, K. N., Hickox, R. C., Greene, J. E., et al. 2014, *ApJ*, 787, 65
- Harrison, C. M., Alexander, D. M., Swinbank, A. M., et al. 2012, *MNRAS*, 426, 1073
- Harrison, C. M., Alexander, D. M., Mullaney, J. R., & Swinbank, A. M. 2014, *MNRAS*, 441, 3306
- Hamann, F. W., Barlow, T. A., Chaffee, F. C., Foltz, C. B., & Weymann, R. J. 2001, *ApJ*, 550, 142
- Heckman, T. M., Armus, L., & Miley, G. K. 1990, *ApJS*, 74, 833
- Humphrey, A., Villar-Martín, M., Sánchez, S. F., et al. 2010, *MNRAS*, 408, L1
- Knigge, C., Scaringi, S., Goad, M. R., & Cottis, C. E. 2008, *MNRAS*, 386, 1426
- Hewett, P. & Foltz, C. 2003, *AJ*, 125, 1784
- Hopkins, P. F., & Elvis, M. 2010, *MNRAS*, 401, 7
- Huchra, J., Latham, D. W., da Costa, L. N., Pellegrini, P. S., & Willmer, C. N. A. 1993, *AJ*, 105, 1637
- Husemann, B., Wisotzki, L., Sánchez, S. F., & Jahnke, K. 2008, *A&A*, 488, 145
- Husemann, B., Wisotzki, L., Jahnke, K., & Sánchez, S. F. 2011, *A&A*, 535, AA72
- Husemann, B., Wisotzki, L., Sánchez, S. F., & Jahnke, K. 2013, *A&A*, 549, AA43
- Kaastra, J. S., Petrucci, P.-O., Cappi, M., et al. 2011, *A&A*, 534, A36
- Kaffe, P. R., Sharma, S., Lewis, G. F., & Bland-Hawthorn, J. 2014, *ApJ*, 794, 59
- Kaspi, S., Smith, P. S., Netzer, H., et al. 2000, *ApJ*, 533, 631
- Kennicutt, R. C., Jr. 1998, *ARA&A*, 36, 189
- Kewley, L. J., Groves, B., Kauffmann, G., & Heckman, T. 2006, *MNRAS*, 372, 961
- Kopylov, I. M., Lipovetskii, V. A., Pronik, V. I., & Chuvaev, K. K. 1974, *Astrofizika*, 10, 483
- Kuzio de Naray, R., Arsenault, C. A., Spekkens, K., et al. 2012, *MNRAS*, 427, 2523
- Landi, E., Young, P. R., Dere, K. P., Del Zanna, G., & Mason, H. E. 2013, *ApJ*, 763, 86
- Landsman, W. B. 1993, *Astronomical Data Analysis Software and Systems II*, 52, 246
- Letawe, G., Magain, P., Courbin, F., et al. 2007, *MNRAS*, 378, 83
- Lipari, S., Sanchez, S. F., Bergmann, M., et al. 2009, *MNRAS*, 392, 1295
- Liu, G., Koda, J., Calzetti, D., Fukuhara, M., & Momose, R. 2011, *ApJ*, 735, 63
- Liu, G., Zakamska, N. L., Greene, J. E., Nesvadba, N. P. H., & Liu, X. 2013a, *MNRAS*, 430, 2327
- Liu, G., Zakamska, N. L., Greene, J. E., Nesvadba, N. P. H., & Liu, X. 2013b, *MNRAS*, 436, 2576
- Liu, G., Calzetti, D., Kennicutt, R. C., Jr., et al. 2013c, *ApJ*, 772, 27
- Liu, G., Calzetti, D., Hong, S., et al. 2013d, *ApJ*, 778, LL41
- Liu, G., Zakamska, N. L., & Greene, J. E. 2014, *MNRAS*, 442, 1303
- Liu, X., Zakamska, N. L., Greene, J. E., et al. 2009, *ApJ*, 702, 1098
- Lucy, A. B., Leighly, K. M., Terndrup, D. M., Dietrich, M., & Gallagher, S. C. 2014, *ApJ*, 783, 58
- McCarthy, I. G. et al. 2010, *MNRAS*, 406, 822
- McElroy, R., Croom, S. M., Pracy, M., et al. 2015, *MNRAS*, 446, 2186
- Meléndez, M., Kraemer, S. B., Schmitt, H. R., et al. 2008, *ApJ*, 689, 95
- Moe, M., et al. 2009, *ApJ*, 706, 525
- Nesvadba, N. P. H., Lehnert, M. D., Eisenhauer, F., et al. 2006, *ApJ*, 650, 693
- Nesvadba, N. P. H., Lehnert, M. D., De Breuck, C., Gilbert, A. M., & van Breugel, W. 2008, *A&A*, 491, 407
- Nesvadba, N. P. H., Polletta, M., Lehnert, M. D., et al. 2011, *MNRAS*, 415, 2359
- Newman, S. F., Buschkamp, P., Genzel, R., et al. 2014, *ApJ*, 781, 21
- Osterbrock, D. E., & Ferland, G. J. 2006, *Astrophysics of Gaseous Nebulae and Active Galactic Nuclei* (2nd. ed.; Sausalito, CA: Univ. Science Books)
- Ostriker, J. P., Choi, E., Ciotti, L., Novak, G. S., & Proga, D. 2010, *ApJ*, 722, 642
- Paturel, G., Petit, C., Prugniel, P., et al. 2003, *A&A*, 412, 45
- Rupke, D. S. N., & Veilleux, S. 2011, *ApJ*, 729, LL27
- Rupke, D. S. N., & Veilleux, S. 2013, *ApJ*, 768, 75
- Shih, H.-Y., & Stockton, A. 2014, *ApJ*, 786, 3
- Sellwood, J. A., & Sánchez, R. Z. 2010, *MNRAS*, 404, 1733
- Silverman, J. D., Lamareille, F., Maier, C., et al. 2009, *ApJ*, 696, 396
- Soker, N. 2010, *MNRAS*, 407, 2355
- Spekkens, K., & Sellwood, J. A. 2007, *ApJ*, 664, 204
- Tabor, G., & Binney, J. 1993, *MNRAS*, 263, 323
- Thomas, H.-C., Beuermann, K., Reinsch, K., et al. 1998, *A&A*, 335, 467
- Tombesi, F., Meléndez, M., Veilleux, S., et al. 2015, *Nature*, 519, 436
- Veilleux, S., Cecil, G., Bland-Hawthorn, J., et al. 1994, *ApJ*, 433, 48
- Véron-Cetty, M.-P., & Véron, P. 2006, *A&A*, 455, 773
- Wood, K. S., Meekins, J. F., Yentis, D. J., et al. 1984, *ApJS*, 56, 507
- Westmoquette, M. S., Clements, D. L., Bendo, G. J., & Khan, S. A. 2012, *MNRAS*, 424, A16
- Whittle, M. 1985, *MNRAS*, 213, 1
- Yaqoob, T., McKernan, B., Kraemer, S. B., et al. 2003, *ApJ*, 582, 105